Dynamic modeling and damage analysis of debris cloud fragments produced by hypervelocity impacts via image processing[*]

Ru ZENG, Yan SONG[‡], Weizhen LV

Department of Control Science and Engineering, University of Shanghai for Science and Technology,

Shanghai 200093, China

E-mail: zengru_neo@163.com; sonya@usst.edu.cn; hala_lwz@163.com

Abstract: It is always a challenging task to model the trajectory and make an efficient damage estimation of debris clouds produced by hypervelocity impact (HVI) on thin-plates due to the difficulty in obtaining high-quality fragment images from experiments. To improve the damage estimation accuracy of HVIs on a typical double-plate Whipple shield configuration, we investigate the distributive characteristic of debris clouds in successive shadowgraphs using image processing techniques and traditional numerical methods. The aim is to extract the target movement parameters of a debris cloud from the acquired shadowgraphs using image processing techniques and construct a trajectory model to estimate the damage with desirable performance. In HVI experiments, eight successive frames of fragment shadowgraphs are derived from a hypervelocity sequence laser shadowgraph imager, and four representative frames are selected to facilitate the subsequent feature analysis. Then, using image processing techniques, such as denoising and segmentation techniques, special fragment features are extracted from successive images. Based on the extracted information, image matching of debris is conducted and the trajectory of debris clouds is modeled according to the matched debris. A comparison of the results obtained using our method and traditional numerical methods shows that the method of obtaining hypervelocity impact experimental data through image processing will provide critical information for improving numerical simulations. Finally, an improved estimation of damage to the rear wall is presented based on the constructed model. The proposed model is validated by comparing the estimated damage to the actual damage to the rear wall.

Key words: Debris clouds; Hypervelocity impact; Image processing; Damage estimation

CLC number: TP301

1 Introduction

With the rapid development of the aerospace industry, more and more human activities are conducted in space, leading to the rapid increase of space trash. Due to the presence of space trash, hypervelocity impact (HVI) events, which have a great potential for damaging spacecraft structures, degrading spacecraft performance, and even leading to disastrous spacecraft accidents, are easily encountered (Summers, 1959; Kessler, 1981). Hence, some specific protection equipment is indispensable for each spacecraft to ensure safety and mission success. The Whipple shield configuration proposed by Fred Whipple in 1947 is a classic protection structure, consisting of a thin bumper plate and a rear

---

wall. When the bumper plate is impacted by a projectile at a tremendous speed, the projectile and the impacted region of the bumper are fragmented due to the extremely high energy-deposition rate of the HVI process. This process produces a backward ejecta debris cloud and a forward debris cloud along the impact direction. Such a debris cloud expands, flies across the standoff, and ultimately reduces the impactor momentum by dispersing the impact over a larger area of the rear wall (Kessler and Cour-Palais, 1978; Yin et al., 2019), and the references therein. Thus, the investigation of debris clouds caused by HVI events is vitally important in shield configuration design and the damage efficiency assessment of space trash, which have gained much attention in recent years (Lambert, 1997; Watson et al., 2017, 2018).

In view of the results of debris clouds in the literature, quite a few achievements are exclusively based on the simulation images. In other words, most debris images for investigation are produced by professional simulation software such as Autodyn. Based on these obtained images, some characteristic parameters (i.e., velocity, angle, and mass) are discussed. In Huang J et al. (2013), a new debris cloud model in terms of the Monte Carlo method was proposed to improve the simulation efficiency. In Wang et al. (2014) and Verma and Dhote (2018), "typical characters of debris have been estimated through the study of the simulation images," and comparisons with damaged plates were provided. However, the production and development of the debris cloud is a complicated dynamic process that is influenced by many factors. Note that debris clouds produced by simulations in the aforementioned literature involve ideal situations, so the desired estimation accuracy cannot be guaranteed. In traditional numerical analysis experiments, the motion and interaction between particles can be simulated, but the shape of the fragment cannot be accurately described. Hence, it is practically essential to make an estimation by analyzing debris clouds derived from experimental tests. Despite its significance, only a few results have been obtained on experimental debris because it is quite difficult to obtain high-quality images (Zhang et al., 2008; Nishida et al., 2013; Huang XG et al., 2016). The works concerning experimental debris, including those outlined above, focus mainly on the investigation of the physical characteristics, where

only a few results with low estimation performance have been obtained. Thus, it is necessary to adopt strategies to extract special information from images to enhance the estimation precision.

Image processing (also called digital image processing), which refers to processing digital images using a computer, aims at improving the visual quality of an image using techniques such as brightness modification, color transformation, enhancement or suppression of certain components, geometric transformation, and extraction of certain features and information contained in the image. In general, image processing includes image transformation, image denoising, image enhancement and restoration, and image segmentation and identification. Although it has a great potential for improving the estimation accuracy, to the best of our knowledge, traditional image processing techniques have seldom been applied to debris analysis, because of the technical difficulties in obtaining essential debris characteristics from a small number of images with rotation and overlap. This motivated us to reduce this scientific gap.

In this study, we investigate the damage and the trajectories associated with the debris clouds produced by HVI through image processing. The main contributions can be highlighted as follows:

1. An advanced photographer, the hypervelocity sequence laser shadowgraph imager, is used to acquire sequential shadowgraphs of a debris cloud with high resolution.

2. Most of the overlapping fragments are separated using the concave point segmentation technique.

3. By analyzing the motion characteristics of fragments and conducting image matching in successive frames of the debris cloud, the trajectory model of matched fragments is successfully established.

4. Damage to the rear wall is effectively estimated based on the established trajectory model by comparing the actual damage pattern of the rear wall and the estimation based on the established model.

2 Source of images

The hypervelocity impact tests are performed on a ballistic range at the China Aerodynamics Research and Development Center (CARDC) (Huang XG et al., 2012, 2013, 2016). As illustrated in Fig. 1, the fundamental structure of the

experimental facility consists mainly of four parts: (1) a two-stage light-gas gun (LGG), (2) an impact chamber within the tested Whipple configuration, (3) a laser-photodetector speed measuring device, and (4) a hypervelocity sequence laser shadowgraph imager. Specifically, the 7.62-mm caliber LGG accelerates a projectile (an aluminum sphere is employed in our experiment) such that hypervelocity (7.36 km/s by this LGG) is obtained at launch. The exact impact velocity of the projectile toward the bumper plates can be obtained at three laser-photodetector stations located along the flight direction. The bumper plates and the rear wall are made of Al-6061 aluminum alloy, whose density and yield strength are 2.73 g/cm^3 and 40 ksi, respectively, and the standoff is set as 80 mm.
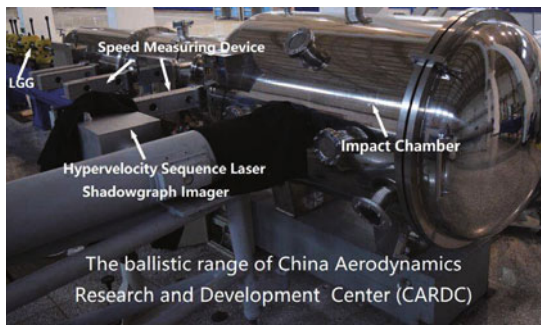

Fig. 1 Facility of the hypervelocity impact experiment

An aluminum alloy sphere with a constant diameter of 2.5 mm is selected as the projectile. Without loss of generality, we set the impact angle, i.e., the angle at which the spherical projectile strikes the bumper, as $\theta = 0°$. The hypervelocity sequence laser shadowgraph imager is employed to record the complete evolution of the debris cloud immediately after the impact on the bumper. The launch speed of the projectile is chosen as 3.24 km/s based on a comprehensive consideration of fairly desirable image quality and available experimental equipment. The purpose is to investigate the trajectories and damage of debris clouds produced by HVIs through image processing.

The following are the three necessary conditions for generating and recording debris clouds in hypervelocity impact experiments (Huang J et al., 2013):

1. A high-velocity projectile is needed, so there is enough kinetic energy to break the projectile and the bumper plates. According to the chosen alu-

minum alloy, the minimum launch velocity is about 3 km/s. Such a requirement is guaranteed by the LGG shown in Fig. 1.

2. The thickness of the bumper plates is in appropriate proportion to the size of the projectile. In other words, the bumper plates cannot be too thick or too thin; otherwise, debris clouds cannot be generated.

3. The camera exposure time of the hypervelocity sequence laser shadowgraph imager should be short enough to capture the shadowgraphs of the debris cloud with high resolution.

According to the above analysis, some important experimental parameters are presented in Table 1.

Table 1 Experimental parameters

Parameter	Value	Unit
Diameter of the projectile	2.5	mm
Thickness of the bumper	1	mm
Thickness of the rear wall	2	mm
Impact velocity of the projectile	3.24	km/s
Distance between two plates	80	mm
Camera exposure time	5	ns

2.1 Images of debris clouds

As stated by Loft et al. (2013) and Huang XG et al. (2014), the morphological feature of debris clouds and the distribution of fragments play critical roles in the damage behavior of the rear wall. Thus, it is important to focus the investigation on the characteristics of the debris cloud and its evolution after impact.

According to Piekutowski (1993) and Huang XG et al. (2016), the debris clouds has three typical structural features: (1) the ejecta veil located ahead of the bumper, (2) the external bubble of debris located inside, and (3) the internal structure at the front of the expanding bubble of the bumper debris. A typical debris cloud is shown in Fig. 2. In our experiment, eight images were obtained by the hypervelocity sequence laser shadowgraph imager every 5 μs (Fig. 3). In Fig. 3, compared with the fragments in the first three and the last images, fragments in the remaining images seldom overlap. Thus, these four successive images were selected for our subsequent investigation. In this study, our goal is to predict the damage to the rear wall by discussing the evolution of the external bubble.

For the chosen four adjacent image frames, according to the camera exposure time given in Table 1, the sampling period between two adjacent frames is 5 ns. It is quite difficult to extract the structural features from the front and edges of the debris cloud, due to the dense aggregation of fragments. In contrast, the characteristics of the main body of the debris cloud can be more easily distinguished.
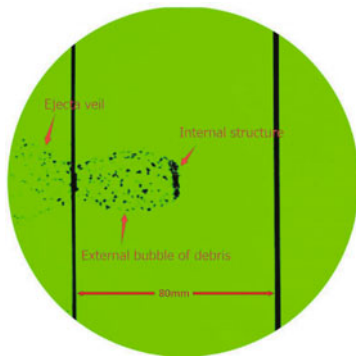

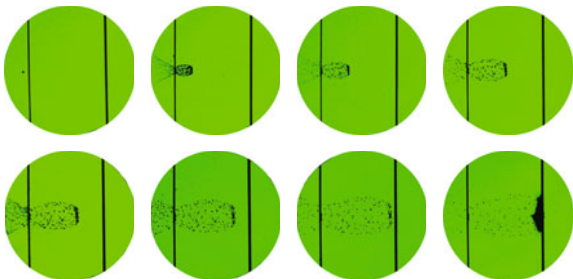**Fig. 2 Structural features of the debris cloud (the size is 150 mm × 150 mm)**

Fig. 3 Raw images of debris clouds (the size is 150 mm × 150 mm)

2.2 Images of the front bumper and rear wall

Figs. 4 and 5 show the damage features of the front bumper and the rear wall after the hypervelocity impact experiment, respectively. Fig. 4 shows a penetrated hole with a diameter of 6 mm in the front bumper; there is curling around this hole due to the plastic deformation of the aluminum alloy. Figs. 5a and 5b demonstrate the front and back surfaces of the rear wall after the hypervelocity impact, respectively. Without loss of generality, for the subsequent performance analysis, we classify the damage patterns into the following three categories (Huang XG

et al., 2014): (1) penetrated hole; (2) main crater; (3) micro-crater. Specifically, the penetrated hole is usually located in the center of the crater zone. The crater is called a main crater if its diameter is larger than 1 mm; otherwise, it is called a micro-crater. The main crater usually gathers in a certain region around the center, while micro-craters spread outside this region.

Fig. 4 The penetrated hole on the front bumper (the size is 170 mm × 114 mm)

In this research, we endeavor to study the characteristics of the debris cloud and craters on the rear wall using image processing techniques. A model composed of the features of the rear wall damage (i.e., crater distribution, crater depth, and crater size) and the features of the debris cloud (i.e., velocity, angle, and distribution) is formulated to establish the relationship between the cloud debris and the rear wall damage.

3 Image processing

3.1 Image pre-processing of the debris cloud

As is well known, image quality plays a central role in image processing due to its great potential for influencing the image segmentation accuracy and image matching rate. Thus, it is usually a primary motivation to obtain high-quality images. To achieve such an objective, pre-processing is conducted to eliminate the noises from raw images of the debris cloud recorded by the hypervelocity sequence laser shadowgraph imager. Because it is technically difficult to obtain three-dimensional (3D) images using the current imager apparatus, the two-dimensional (2D) images of the fourth to the seventh subfigures in Fig. 3 were used instead, which implies that the depth information is missing in the studied images. In what follows, the detailed image pre-processing
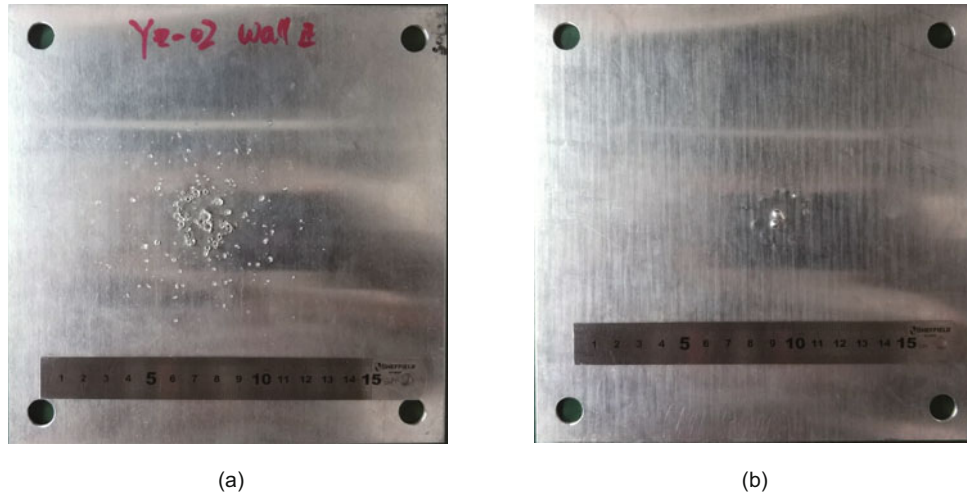
Fig. 5 Surfaces of the rear wall after hypervelocity impact (the size is 200 mm × 200 mm): (a) front surface; (b) back surface

procedure for each frame is presented.

It is obvious that these four raw images include both the debris cloud and its background. For better analysis, the original images were first cropped to delete the redundant parts that did not cause damage to the rear wall, such as the backsplash debris cloud, and only the forward debris cloud images between the front bumper and the rear wall were retained. Then the cropped images were converted into grayscale images that carried only intensity information. Aiming at removing the noises in grayscale images, while retaining edge information, a bilateral filter was adopted, where the intensity of each pixel is replaced by the weighted average of the intensity values from nearby pixels. Finally, a so-called morphological operation, i.e., an opening operation, was performed to deal with some remaining noise in images. In this sense, fragments with more than 1000 pixels or fewer than 100 pixels are removed.

3.2 Image segmentation of debris clouds

Image segmentation is the process of partitioning a digital image into multiple segments, such as sets of pixels. The goal of segmentation is to simplify or change the representation of an image into certain items that are more meaningful and easier to analyze. More precisely, image segmentation is the process of assigning a label to every pixel in an image so that pixels with the same label share certain characteristics. In this subsection, because the numerous fragments with a small number of pixels could reduce the accuracy and increase the computation overhead of the matching process in Section 3.3, we first used threshold segmentation to filter the small pieces of fragments in the debris cloud. Next, we adopted concave point segmentation to segment the overlapping fragments, which could be split into several smaller fragments in the successive images, to further improve the matching accuracy.

To segment fragments into different regions with respect to their image features, threshold value segmentation is used to handle fragments of debris clouds, which is applicable by selecting a constant "T," and enjoys an essential position in applications of image segmentation because of intuitive properties, ease of implementation, and high computational speed (Masters et al., 2009). A fixed global threshold is selected to separate modes of images as shown in Fig. 6. Note that most of the fragments are successfully segmented with the help of threshold value segmentation.

In this study, we endeavor to extract target movement parameters of the debris cloud from the acquired shadowgraphs via image processing. Images generated by the hypervelocity sequence laser shadowgraph imager are 2D, and thus depth information is missing. Thus, overlapping of debris is a serious problem for the subsequent feature extraction. Although there are some fragments at the head of the debris images, it is a big challenge to

extract useful information, which leads to problems for image matching. Thus, some debris images were removed before image matching. In Fig 6, images include all the fragments, while Fig. 7 describes only key fragments of debris clouds. Notice that the number of fragments in the first three frames increases gradually, while the fragment quantity of the last frame decreases. This is because some fragments are further split into small pieces whose contours have far fewer than 100 pixels. These small fragments are deleted.
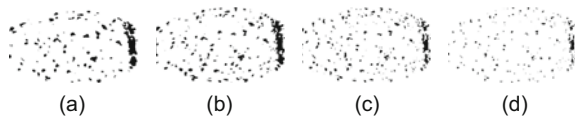

Fig. 6 Fragments of debris clouds after pre-processing (the size is 80 mm × 53 mm). (a)−(d) correspond to the fourth to seventh subfigures in Fig. 3 after pre-processing

Fig. 7 Key fragments of debris clouds after pre-processing (the size is 80 mm × 53 mm). In (a)−(d), the number of fragments is 60, 90, 109, and 90, respectively

However, there are a few seriously adhering/overlapping fragments in Fig. 7a, which cannot be divided directly. To handle this problem, concave point segmentation, proposed by Fu et al. (2007) and Yin et al. (2020), is further employed. Specifically, the concave point segmentation algorithm aims at finding the concave point at the contour's edge in the overlapping region and dividing overlapping regions based on separating points obtained from concave points. Fig. 8 describes the result of Fig. 7a after concave point segmentation, where the short red line notes the separation of fragments.

Based on matched fragments, in the next subsection, we will try to extract target movement parameters of debris clouds from Fig. 7 to establish the motion model of the debris clouds.

3.3 Image matching of debris clouds

Image matching is a method of finding the target in similar images by analyzing the correspondence, similarity, features, and consistency of the

Fig. 8 Results of Fig. 7a by concave point segmentation (the size is 80 mm × 53 mm). References to color refer to the online version of this figure

content. In this sense, the same fragments in two successive images would be matched. Because they have great invariant features on image translation, scaling, and rotation, moment invariants, which include, but are not limited to, geometric moments, Zernike moments, rotational moments, and complex moments (Teague, 1980), have been used to conduct image matching for fragments. In recent years, moments and the related invariants have been extensively used to characterize image patterns in various applications.

Moment invariants were originally proposed in Hu (1962), where the author obtained six absolute orthogonal invariants and one skew orthogonal invariant through algebraic invariants. These moment invariants related to position, size, orientation, and parallel projection have great potential in tracing image patterns under the assumption that images are continuous functions and noise-free. Because the same fragment in the debris cloud would change the direction and position, it is hard for us to directly match the fragments in two successive images. Therefore, the moment invariants are employed for image processing of debris clouds.

Consider the following 2D $(m+n)^{\text{th}}$-order moment (Huang ZH and Leng, 2010):

$$\mathcal{M}_{mn} = \int_{-\infty}^{\infty} \int_{-\infty}^{\infty} x^m y^n f(x,y) \mathrm{d}x\mathrm{d}y,$$
$$m, n = 0, 1, 2, \cdots , \qquad (1)$$

where $f(x,y)$ is the image function. Obviously, the moments of all orders will exist if the function $f(x,y)$ is piecewise continuous and bounded. Furthermore, the moment sequence denoted by $\mathcal{M}_{mn}$ is exclusively determined by $f(x,y)$, and vice versa.

Note that moments in Eq. (1) might not be invariant if $f(x,y)$ changes during translation,

rotation, or scaling. In this sense, by using central moments, the following invariant features can be obtained:

$$\mathcal{C}_{mn} = \int_{-\infty}^{\infty}\int_{-\infty}^{\infty}(x-\bar{x})^m(y-\bar{y})^n f(x,y)\mathrm{d}x\mathrm{d}y,$$
$$m, n = 0, 1, 2, \cdots, \tag{2}$$

where the pixel point $(\bar{x}, \bar{y})$, defined by $\bar{x} = \frac{\mathcal{M}_{10}}{\mathcal{M}_{00}}$, $\bar{y} = \frac{\mathcal{M}_{01}}{\mathcal{M}_{00}}$, is the centroid of the image $f(x,y)$. The centroid moments, $\mathcal{C}_{mn}$, calculated by $(\bar{x}, \bar{y})$ are equivalent to moments $\mathcal{M}_{mn}$ obtained by shifting their center to the centroid of the image (Teague, 1980). Thus, the centroid moments are invariant against image translations, which can be defined by the following normalized form:

$$\nu_{mn} = \frac{\mathcal{C}_{mn}}{\mathcal{C}_{00}^{\lambda}}, \lambda = \frac{m+n+2}{2}, \ m+n = 2, 3, \cdots. \tag{3}$$

Based on the obtained centroid moments, seven moment invariants have been developed for fulfilling image matching (Hu, 1962):

$$\begin{cases} \varphi_1 = \nu_{20} + \nu_{02}, \\ \varphi_2 = (\nu_{20} - \nu_{02})^2 + 4\nu_{11}^2, \\ \varphi_3 = (\nu_{30} - 3\nu_{12})^2 + (3\nu_{21} - \mathcal{C}_{02})^2, \\ \varphi_4 = (\nu_{30} + \nu_{12})^2 + (\nu_{21} + \mathcal{C}_{03})^2, \\ \varphi_5 = (\nu_{30} - 3\nu_{12})(\nu_{30} + \nu_{12})(\nu_{30} + \nu_{12})^2 \\ \qquad - 3(\nu_{30} - 3\nu_{12})(\nu_{30} + \nu_{12})(\nu_{21} + \nu_{03})^2 \\ \qquad + 3(3\nu_{21} - \nu_{03})(\nu_{21} + \nu_{03})(\nu_{30} + \nu_{12})^2 \\ \qquad - (3\nu_{21} - \nu_{03})(\nu_{21} + \nu_{03})(\nu_{21} + \nu_{03})^2, \\ \varphi_6 = (\nu_{20} - \nu_{02})\left[(\nu_{30} + \nu_{12})^2 - (\nu_{21} + \nu_{03})^2\right] \\ \qquad + 4\nu_{11}(\nu_{30} + \nu_{12})(\nu_{21} + \nu_{03}), \\ \varphi_7 = (3\nu_{21} - \nu_{03})(\nu_{30} + \nu_{12})(\nu_{30} + \nu_{12})^2 \\ \qquad - 3(\nu_{21} + \nu_{03})^2(3\nu_{21} - \nu_{03})(\nu_{30} + \nu_{12}) \\ \qquad - 3(\nu_{30} - 3\nu_{12})(\nu_{21} + \nu_{03})(\nu_{30} + \nu_{12})^2 \\ \qquad + (\nu_{30} - 3\nu_{12})(\nu_{21} + \nu_{03})(\nu_{21} + \nu_{03})^2. \end{cases} \tag{4}$$

Obviously, the above seven moments are also invariant against image scaling, translation, and rotation.

In this research, image matching is achieved using the matchshape function, which is a traditional function in the OpenCV function library. Specifically, the matchshape function uses contours of fragments to calculate their similarity. The smaller such a value is (i.e., the closer to zero the returned value

is), the more similar the addressed contours will be. Figs. 9 and 10 show the image matching results of two pairs of adjacent fragments in terms of the aforementioned invariant moments on OpenCV, i.e., between Figs. 7a and 7b and between Figs. 7b and 7c, respectively. As depicted in Figs. 9 and 10, each pair of matched debris is labeled with the same number, while solid debris is mismatched. From Figs. 9 and 10, the matching efficiency of each pair of adjacent fragments is about 50%.

3.4 Trajectory of debris

It is always difficult to fulfill trajectory prediction of debris because the rotation and the overlapping of fragments might happen while they are approaching the rear wall. So far, only a few results have been reported in the literature. In Watson et al. (2017), a random sample consensus (RANSAC) algorithm was developed for linear fitting with respect to all the fragment positions. Although they proposed an effective strategy for the prediction of the debris trajectory, it is difficult to achieve high-accuracy prediction in the presence of overlapping and rotation of debris and the random feature of RANSAC. To overcome these obstacles, representative fragments are used instead of all fragments to make a better trajectory prediction. Specifically, by comparing the matching results of Fig. 9b with those of Fig. 10a, the commonly matched fragments are chosen as objectives for image matching. Based on these obtained objectives, we extract their corresponding fragments from Figs. 9a and 10b, while deleting the rest. Then, the centroid of decisive fragments is calculated as shown in Fig. 11.

Note that the external forces acting on fragments are sufficiently small to be negligible. Specifically, deceleration resulting from aerodynamic drag is trivial in the vacuum circumstance of the experimental chamber. The gravity is also negligible during such a micro-second process. According to the above discussions, the general external forces are neglected during the investigation of image matching. By linking these matched fragments based on the centroid coordinates in Fig. 11, the evolutionary trajectories of fragments in the xy plane are desirably obtained (Fig. 12).

Fig. 9 Image matching of adjacent fragments (the size is 80 mm × 53 mm): (a) results of Fig. 7a; (b) results of Fig. 7b

Fig. 10 Image matching of adjacent fragments (the size is 80 mm × 53 mm): (a) results of Fig. 7b; (b) results of Fig. 7c
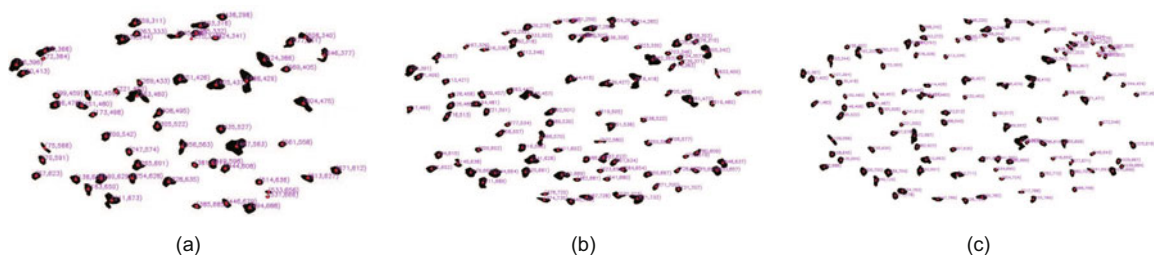

Fig. 11 Centroids of the matched debris of adjacent images (the size is 80 mm × 53 mm): (a) centroids of the fragments in Fig. 7a; (b) centroids of the fragments in Fig. 7b; (c) centroids of the fragments in Fig. 7c

3.5 Image processing of the front surface of the rear wall

To precisely analyze the damage level of the rear wall, which was filled with many contiguous craters, we needed to extract image features of Fig. 5a first, which is somewhat challenging due to the reflection from the material of the rear wall. In addition, it is difficult to directly extract the contours of the main craters due to the surrounding scratches generated by the fragments ejected from the front bumper. Unfortunately, traditional image processing methods, such as threshold and watershed segmentation, are invalid for handling these images. The intensity of the image is used instead to indirectly obtain the contour information.

As far as the intensity is concerned, the HSI color method proposed by Munsell (1939) and Birren (1969) has great potential for describing the color perception, and has thus gained much attention in
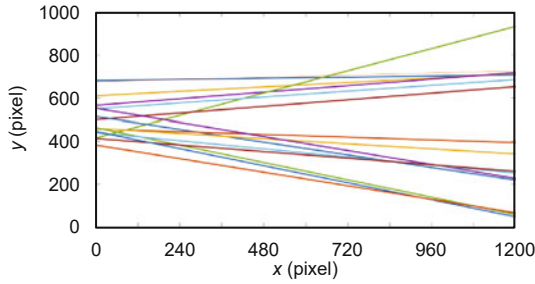
Fig. 12 Trajectory of matched debris

recent years (Chein and Tseng, 2011; Kamiyama and Taguchi, 2021). In an additive color system, the RGB format is often used to specify a color according to three different electron guns like red, green, and blue, whereas in the human visual system, color images are always perceived in terms of hue, saturation, and luminance, thereby leading to the HSI format (i.e., hue, saturation, and intensity). In line with Li JF et al. (2002) and Jayashree (2013), the conversion equation from the RGB space to the HSI space is

$$
\begin{cases}
I = \sqrt{3}(\mathcal{R} + \mathcal{G} + \mathcal{B}), & \text{(5a)} \\
\theta = \arccos\!\left(\dfrac{(\mathcal{R} - \mathcal{G}) + (\mathcal{R} - \mathcal{B})}{2\sqrt{(\mathcal{R} - \mathcal{G})^2 + (\mathcal{R} - \mathcal{B})(\mathcal{G} - \mathcal{B})}}\right), & \\
& \text{(5b)} \\
H = \begin{cases} \theta, & \mathcal{G} \geq \mathcal{B}, \\ 2\pi - \theta, & \mathcal{G} < \mathcal{B}, \end{cases} & \text{(5c)} \\
S = 1 - \dfrac{3\min(\mathcal{R}, \mathcal{G}, \mathcal{B})}{\mathcal{R} + \mathcal{G} + \mathcal{B}}, & \text{(5d)}
\end{cases}
$$

where H denotes a pure color in the context of an angle function defined for the polar coordinate system, S in a linear proportion to the radial distance stands for the color purity, and I, denoted by the distance from the axis perpendicular to the polar coordinate, is the brightness.

The following are specific steps for processing the rear wall image:

1. Transform the image in the RGB format to the HSI format.

2. Set an appropriate threshold of the I component to achieve desirable image results through segmentation.

3. Remove noises using a Gaussian filter, and extract the inner edges of craters.

4. Delete trivial scratches by applying a continuous open operation.

5. Calculate the centroid of every contour.

In terms of HSI models for Fig. 5a, Figs. 13–16 show the corresponding results by using Eqs. (5a)–(5d).

Fig. 13 Binary image of the rear wall (the size is 2000 mm × 2000 mm)

Fig. 14 All craters in the image of the rear wall (the size is 2000 mm × 2000 mm)

Fig. 15 Main contours of craters (the size is 2000 mm × 2000 mm)

Fig. 16 Centroids of contours of craters in Fig. 15 (the size is 2000 mm × 2000 mm)

4 Results

Based on the information established so far, we are ready to estimate the degree of debris damage to the rear wall. To the best of the authors' knowledge, there are few results on the features (e.g., velocity and angle) in the literature due to the technical difficulties in handling debris cloud images. Only a few investigations on the evolution of debris cloud expansion have been reported in recent years (Li HX et al., 2016). However, the previously mentioned characteristics usually play a central role in damage estimation. It is therefore important to extract this debris information using image processing techniques. In the following, for the fourth to the seventh subfigures in Fig. 3, the detailed procedure for obtaining data such as velocity and angle is presented step by step.

In Huang J et al. (2013), a debris cloud model based on statistical results was proposed, including the distribution functions of velocity and leap angles. We compare the results obtained in our study with those obtained by the method in Huang J et al. (2013).

4.1 Distribution of debris velocity

Among the four successive images in Figs. 7a–7d, the fragments of the last two successive images (i.e., Figs. 7c and 7d) seldom overlapped; thus, they were used to estimate the velocity of debris. First, image matching was applied to Figs. 7c and 7d. Second, using the moment invariant technique, the centroid of each pair of matched fragments denoted by hollow circles in Figs. 17a and 17b was obtained.

Moreover, in combination with the time interval

of the two images, the velocity of debris was derived. On one hand, as depicted in Fig. 10, each matched debris pair was labeled with the same number. We can also use central moments to calculate every centroid of the matched debris. On the other hand, the external forces acting on fragments were sufficiently minimal to be negligible in experiments. Specifically, deceleration resulting from aerodynamic drag was trivial in the vacuum circumstance of the experimental chamber. The gravity was also negligible during this micro-second process. Thus, the general external forces were neglected during image matching. Based on the time interval between every two adjacent images and the position information, the velocities of matched fragments were easily obtained. The distribution of the matched fragment velocities is shown in Fig. 18. It is obvious that the velocities of most of the fragments were about 1.08–1.44 km/s, much lower than the impact velocity of the projectile, or 3.24 km/s. This implied that the damage to the front wall was more serious than the damage to the rear wall, which is well illustrated in Figs. 5a and 5b.

In Huang J et al. (2013), the normalized debris velocity accumulation number $\mathrm{CN}(v)$ was defined as the ratio of the number of debris fragments with a relative velocity less than v to the total number of debris fragments:

$$\mathrm{CN}(v) = \frac{\sum_{v'=0}^{v'=v} n(v')}{\sum_{v'=0}^{v'=v_{\max}} n(v')}, \qquad (6)$$

where $n(v')$ is the number of debris fragments ejected with the relative velocity, v', and v is the debris relative velocity, which is the ratio of the debris velocity to $V_{\max}$. The distribution function of $\mathrm{CN}(v)$ in v space can be expressed as follows:

$$\mathrm{CN}(v) = v^{0.895}. \qquad (7)$$

We want to use the distribution functions of the debris velocity to verify the validity of the data in Fig. 10. In Fig. 19, the red line represents Eq. (7), and the green stars represent the results of fitting the data in Fig. 10. We can see that $\mathrm{CV}(v)$ increases as the debris relative velocity v increases. We fit the data in Fig. 10 using the same functional form as in Eq. (2) and represent it in green in Fig. 19. We can see that the velocity data obtained in this study is similar to the numerical analysis results.
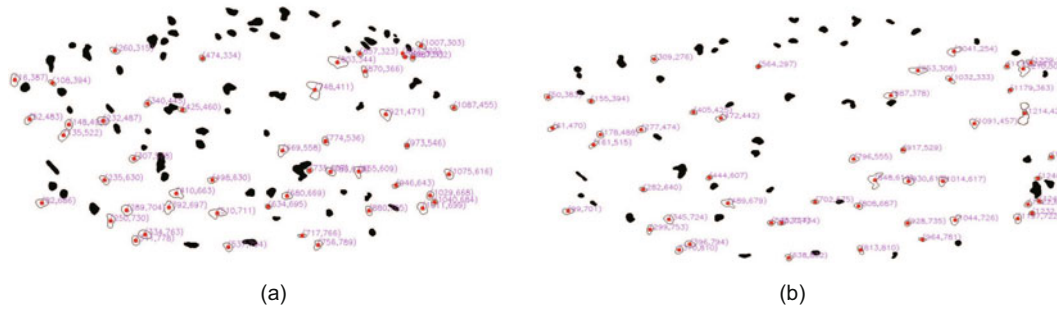
Fig. 17 Centroids of fragments of the last two successive images (the size is 80 mm × 53 mm): (a) centroids of fragments in Fig. 7c; (b) centroids of fragments in Fig. 7d
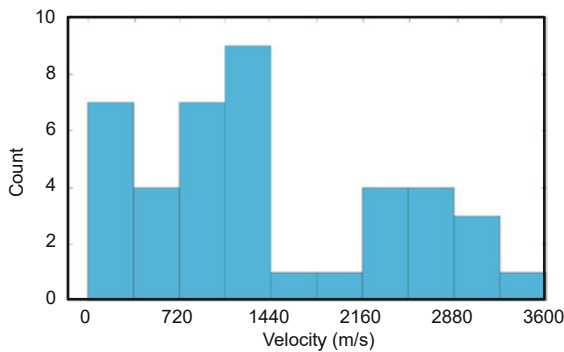

Fig. 18 Velocity distribution of fragments

The new distribution function in our study, $CN(v)$, can be expressed as follows:

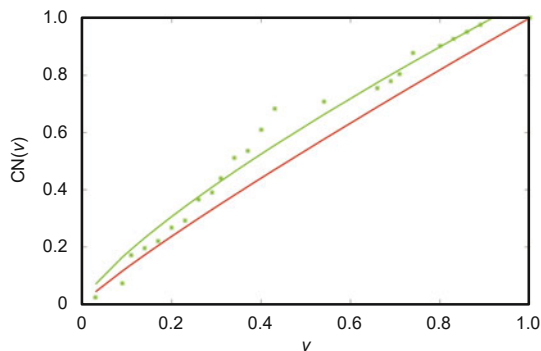$$CN(v) = 1.07v^{0.778}. \tag{8}$$

Fig. 19 Debris velocity comparison (References to color refer to the online version of this figure)

4.2 Distribution of the debris leap angle

According to the centroids of the matched fragments depicted in Fig. 17, the distribution of leap angles of these fragments is shown in Fig. 21, where

the leap angle is defined by angles between the debris position vector and the positive direction of the y axis. We can see the sketched map of the leap angle in Fig. 20. From Fig. 21, the number of fragments with angles in the range of $[80°, 100°]$ is over 50% of the total. This means that quite a few fragments hit the rear wall, resulting in great potential for serious damage.
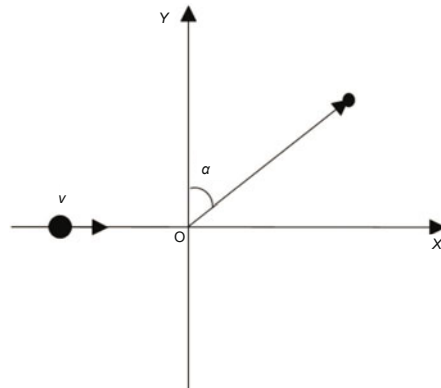

Fig. 20 Definition of the leap angle of a debris particle

In Huang J et al. (2013), $n(\alpha)$ was defined as the ratio of the number of debris fragments with angle α to the total number of debris fragments. The debris distribution function $n(\alpha)$ in α space can be written as Eq. (9), with w_α being 22.5:

$$n(\alpha) = \exp\left[-2\left(\frac{\alpha - 90}{w_\alpha}\right)^2\right] \Big/ \left(w_\alpha\sqrt{\frac{\pi}{2}}\right). \tag{9}$$

We used the same method as in Section 4.1 to verify the validity between the numerical analysis results and the data obtained in this study. In Fig. 22, the green line represents the numerical analysis result of Eq. (9), and the blue

line represents the distribution of the leap angles obtained in this study. We can see that the distribution of leap angles is concentrated mainly in $[80°, 100°]$, for both the numerical derivation results and the results obtained in our study.

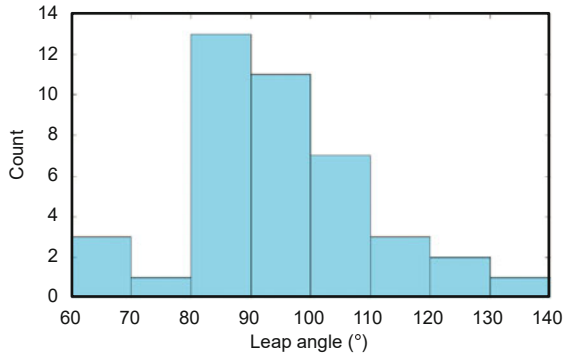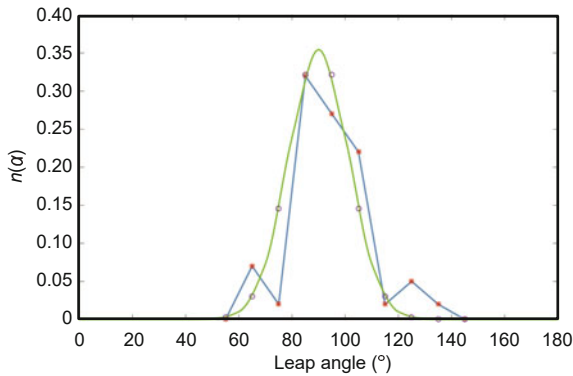**Fig. 21 Distribution of fragment leap angles**

Fig. 22 Leap angle comparison (References to color refer to the online version of this figure)

4.3 Matched fragments with k-means clustering

To further analyze the debris features, a k-means clustering algorithm was used to deal with the position and leap angle data of matched fragments in the last two successive images, Figs. 17a and 17b. The main idea of this algorithm is to separately define k centroids for k clusters. To be more specific, $X = \{x_i \mid i = 1, 2, ..., n\}$, the set of n d-dimensional points, is required to be clustered into a set of k clusters, i.e., $C = \{c_j \mid j = 1, 2, ..., k\}$. The k-means algorithm is designed to find a partition such that the objective function (usually defined by a squared error between the points and their mean, also called the centroid of a cluster) is minimized (Jain, 2010).

Define $\tilde{c}_j$ as the mean of cluster c_j. The squared error between $\tilde{c}_j$ and the points in cluster c_j is determined by

$$J_j = \sum_{x_i \in c_j} \|x_i - \tilde{c}_j\|^2. \tag{10}$$

The k-means algorithm aims at minimizing the sum of the squared error over all k clusters. Thus, the general objective function is given by

$$J = \sum_{j=1}^{k} \sum_{x_i \in c_j} \|x_i - \tilde{c}_j\|^2. \tag{11}$$

Fig. 23 describes the performance of different numbers of clusters. It is obvious that four clusters lead to the best performance. Thus, matched fragments are clustered in four clusters by the k-means clustering algorithm, and the results are given in Fig. 24. From Fig. 24, the number of fragments with an angle between $-10°$ and $10°$ is 24, which is about 65% of the 37 underlying matched fragments. To conclude, the results shown in Fig. 24 are similar to those in Fig. 21.
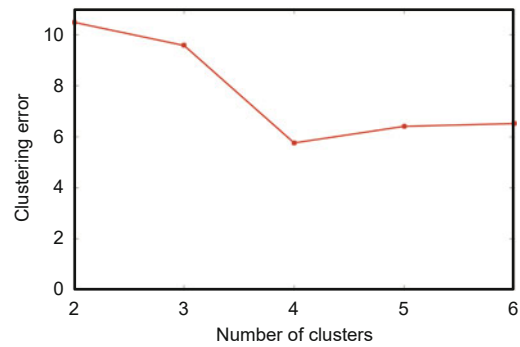

Fig. 23 Performance of different numbers of clusters

4.4 Trajectory of the fragment and impacting position

Next, we will analyze the damage on the rear wall based on the extracted main contours of craters described by Fig. 15. By calculating 114 craters on the rear wall, the areas of these craters are directly obtained. Their distribution is shown in Fig. 25. It is clear that there are 50 craters with an area between 0 and 2 mm^2, almost half of the total. In addition, the contour of debris clouds keeps enlarging. By searching the convex hulls (i.e., minimum convex polygons)
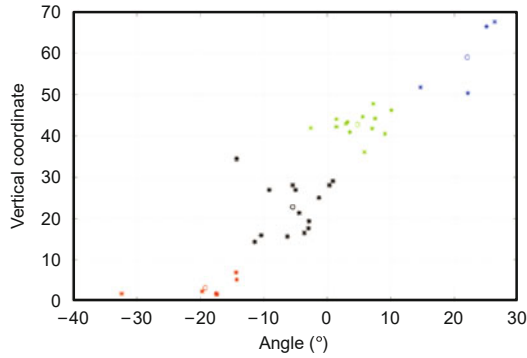
Fig. 24 Matched fragments with *k*-means clustering

for two series of successive images, the area evolution of the debris clouds can be obtained.
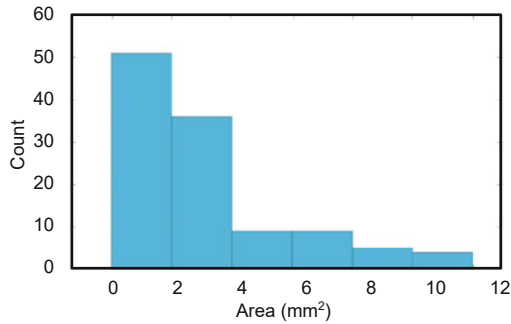

Fig. 25 Area distribution of craters

Now we are ready to estimate the positions where fragments reach the rear wall. To illustrate the efficiency and accuracy of our prediction, the evolution of matched fragments on the xy plane and the distribution of craters projected in the vertical axis are both taken into consideration. Based on Figs. 12 and 16, the results are given in Fig. 26. The colorful dots located in the vertical axis represent the trajectory endpoints of all fragments, wherein red dots denote the main craters of severe damage. From Fig. 26, we can easily find that the arriving positions of matched fragments belong to such a domain comprising the main craters. We can see that the trajectories originate from a relatively concentrated area. This means that the perforation size of the front plate is almost 9 mm. In Fig. 4, we can see that the actual perforation size of the front plate is almost 8 mm. This is similar to the result obtained by our method. As another example, in Fig. 21, more than 50% of the fragments have angles in the range of [80°, 100°]. In Fig. 26, the leap angles of

most trajectories are distributed in this range. This demonstrates that our method is valid. In our future work, we can further investigate these matched fragments to estimate the damages resulting from the hypervelocity impact.
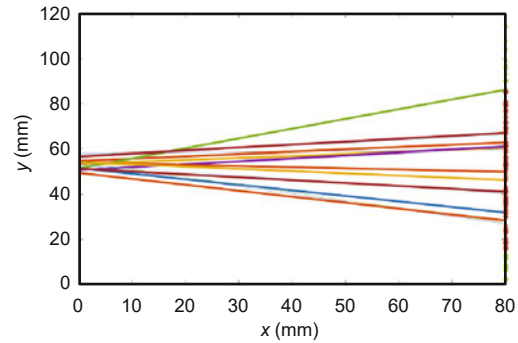

Fig. 26   Trajectories of the fragments and impacting positions (References to color refer to the online version of this figure)

5 Discussion

From the experimental results, with proper image processing, the resulting trajectory model can obtain high accuracy when predicting damage to the rear wall. Next, we discuss the pros and cons of our methods compared to others. In this study, we investigate the trajectory modeling and the damage estimation of debris clouds generated by HVIs. By using image processing techniques, certain features of fragments have been extracted from successive shadowgraphs of the debris cloud. So far, only a few results have been reported in the literature. Most of papers on debris cloud modeling are based on existing numerical theory models, and few methods of modeling have used image processing.

The main reason is that it is difficult for common equipment to obtain a sequence of high-quality images under the experimental condition of hypervelocity impacts. In Watson et al. (2017), a RANSAC algorithm was developed for linear fitting with respect to all the fragment positions. However, the high accuracy of the prediction is probably the result of an ideal scenario in the presence of overlapping and rotation of debris. The relationship between the same fragments in two adjacent images is not easily found. Fragments are tracked based not on the shape, feature, or brightness, but on the

position. To overcome these obstacles, representative fragments based on image matching are used to predict the trajectory, instead of using all fragments. The performance size of the front plate is almost 9 mm, very similar to the actual size of about 8 mm. This demonstrates that our method is valid.

Compared with traditional prediction models for investigating debris produced in HVI experiments, there are mainly two differences in our proposed model—one is purpose, and the other is the modeling technique. For the addressed models, the main purpose of the traditional Piekutowski model is to obtain the velocity information in various debris cloud directions using the momentum conservation theorem. Schonberg's model aims at obtaining the velocity distribution of debris clouds by separating the debris of the projectile and that of the bumper plate. In contrast, this study aims at modeling the dynamics of debris clouds using image processing techniques and estimating damage based on this established model. In addition, the Piekutowski and Schonberg models are physical models that are constructed using the impact velocity and the mass of the projectile. These two models seldom investigate the relationship of successive images of debris clouds. The trajectory model proposed in this study is constructed using image processing techniques. It is challenging due to the difficulties in obtaining high-quality images and extracting useful information from images.

In traditional numerical analysis, the motion and interaction between particles can be simulated, but the shape of the fragment cannot be accurately described. For example, we also used the method of smoothed particle hydrodynamics (SPH) to simulate the projectile and target. This is why experimental data on fragmentation is key information for improving the simulations. Data measured with this technique allows for more in-depth studies of hypervelocity impact fragmentation phenomena and will provide an excellent source of information for directly validating numerical simulations. In Section 4, we did some comparisons with the results of numerical analysis. We used the equations of the distribution of velocity and leap angle in Huang J et al. (2013) to verify the validity of the values in our study. The results in our study were consistent with those we derived numerically. In summary, the proposed method is effective, but the analysis results

provided are relatively limited. In the future, we will continue to improve our algorithms to increase the amount and accuracy of data.

The main limitation of our method is the image quality. This is especially important in experiments at higher velocities, where fragments will be small, or even molten droplets. In this study, we can find the same fragment in two successive images using image processing techniques. We extract mainly the invariant features by analyzing the corresponding characteristics of the fragments. The higher image quality is critical for capturing the image features of the fragment. Although our method can be used in most normal cases, an image with low quality will lead to poor accuracy of the established motion model. Therefore, if the quality of the photos is not good enough, the effectiveness of the algorithm will be greatly affected. The choice of 3.24 km/s as the impact velocity in this study is based mainly on the consideration of the available image quality and existing experimental equipment. If the equipment and experimental conditions are improved in the coming future, a higher impact velocity will be our preferred choice.

Currently, we can establish only a trajectory model of a debris cloud in the 2D space. The reason why we cannot establish a 3D trajectory model is that the photo taken by the hypervelocity sequence laser shadowgraph imager is a 2D image. Some depth information of debris is missing in the 2D images. We believe that upgrades in the experimental equipment will allow the debris cloud image quality to be improved. We will try to create a 3D motion model by taking a series of debris images from multiple hypervelocity sequence laser shadowgraph imagers with different visual angles.

6 Conclusions

In this study, we investigated the trajectory modeling and damage estimation of debris clouds generated by HVIs. Using several image processing techniques, certain features of fragments were extracted from successive shadowgraphs of debris clouds. Then, by image matching, the trajectory of debris was modeled with respect to the derivatives. Based on the established model, the damage to the rear wall was estimated, and the effectiveness of the proposed model was demonstrated by comparison

with the actual damage to the rear wall. Finally, a comparison of the results obtained using our method and traditional numerical methods validates the effectiveness of the method of obtaining hypervelocity impact experimental data through image processing, and this method will provide critical information for improving numerical simulations. In future work, we will deal with image problems such as overlapping and rotation to further improve the estimation accuracy, and provide multiple data to improve the numerical simulations.

Contributors

Yan SONG designed the research. Ru ZENG and Weizhen LV processed the images. Ru ZENG drafted the paper. Yan SONG helped organize the paper. Ru ZENG and Weizhen LV revised and finalized the paper.

Compliance with ethics guidelines

Yan SONG, Ru ZENG, and Weizhen LV declare that they have no conflict of interest.

References

Birren F, 1969. A Grammar of Color (A Basic Treatise on the Color System of Albert H. Munsell). van Nostrand Reinhold Co., New York, USA.

Chein CL, Tseng DC, 2011. Color image echancement with exact HSI color model. *Int J Innov Comput Inform Contr*, 7(12):6691-6710. https://doi.org/10.1093/imamci/dnr018

Fu R, Shen H, Chen H, 2007. Research of automatically separating algorithm for overlap cell based on searching concave spot. *Comput Eng Appl*, 43(17):21-23 (in Chinese).

Hu MK, 1962. Visual pattern recognition by moment invariants. *IRE Trans Inform Theory*, 8(2):179-187. https://doi.org/10.1109/TIT.1962.1057692

Huang J, Ma ZX, Ren LS, et al., 2013. A new engineering model of debris cloud produced by hypervelocity impact. *Int J Impact Eng*, 56:32-39. https://doi.org/10.1016/j.ijimpeng.2012.07.003

Huang XG, Zhang L, Zhao ZM, et al., 2012. Microstructure transformation and mechanical properties of TiC-TiB$_2$ ceramics prepared by combustion synthesis in high gravity field. *Mater Sci Eng A*, 553:105-111. https://doi.org/10.1016/j.msea.2012.05.099

Huang XG, Zhao ZM, Zhang L, 2013. Fusion bonding of solidified TiC-TiB$_2$ ceramic to Ti-6Al-4V alloy achieved by combustion synthesis in high-gravity field. *Mater Sci Eng A*, 564:400-407. https://doi.org/10.1016/j.msea.2012.12.005

Huang XG, Zhao ZM, Zhang L, et al., 2014. Microstructure modification and fracture behavior of solidified TiC-TiB$_2$ ceramic prepared by combustion synthesis in ultra-high gravity field. *J Asian Ceram Soc*, 2(2):144-149. https://doi.org/10.1016/j.jascer.2014.02.003

Huang XG, Yin C, Huang J, et al., 2016. Hypervelocity impact of TiB$_2$-based composites as front bumpers for space shield applications. *Mater Des*, 97(5):473-482. https://doi.org/10.1016/j.matdes.2016.02.126

Huang ZH, Leng JS, 2010. Analysis of Hu's moment invariants on image scaling and rotation. Proc 2nd Int Conf on Computer Engineering and Technology, p.V7-476-V7-480. https://doi.org/10.1109/ICCET.2010.5485542

Jain AK, 2010. Data clustering: 50 years beyond K-means. *Patt Recogn Lett*, 31(8):651-666. https://doi.org/10.1016/j.patrec.2009.09.011

Jayashree RA, 2013. RGB to HSI color space conversion via MACT algorithm. Proc Int Conf on Communication and Signal Processing, p.561-565. https://doi.org/10.1109/iccsp.2013.6577117

Kamiyama M, Taguchi A, 2021. Color conversion formula with saturation correction from HSI color space to RGB color space. *IEICE Trans Fundam Electron Commun Comput Sci*, E104.A(7):1000-1005. https://doi.org/10.1587/transfun.2020EAL2087

Kessler DJ, 1981. Sources of orbital debris and the projected environment for future spacecraft. *J Spacecr Rock*, 18(4):357-360. https://doi.org/10.2514/3.57828

Kessler DJ, Cour-Palais BG, 1978. Collision frequency of artificial satellites: the creation of a debris belt. *J Geophys Res Space Phys*, 83(A6):2637-2646. https://doi.org/10.1029/JA083iA06p02637

Lambert M, 1997. Hypervelocity impacts and damage laws. *Adv Space Res*, 19(2):369-378. https://doi.org/10.1016/S0273-1177(97)00027-6

Li HX, Tao JL, Lu YG, 2016. Glass debris cloud contour extend calculation method research under the explosion. *J Ordnan Equip Eng*, 37(5):129-134 (in Chinese). https://doi.org/10.11809/scbgxb2016.05.031

Li JF, Wang KQ, Zhang D, 2002. A new equation of saturation in RGB-to-HSI conversion for more rapidity of computing. Proc Int Conf on Machine Learning and Cybernetics, p.1493-1497. https://doi.org/10.1109/ICMLC.2002.1167456

Loft K, Price MC, Cole MJ, et al., 2013. A new online resource for the hypervelocity impact community and the change of debris cloud impact patterns with impact velocity. *Proc Eng*, 58:508-516. https://doi.org/10.1016/j.proeng.2013.05.058

Masters BR, Gonzalez RC, Woods RE, 2009. Book review: digital image processing, third edition. *J Biomed Opt*, 14(2):029901. https://doi.org/10.1117/1.3115362

Munsell AH, 1939. A Color Notation (8th Ed.). Munsell Color Company, Baltimore, USA.

Nishida M, Kato H, Hayashi K, et al., 2013. Ejecta size distribution resulting from hypervelocity impact of spherical projectiles on CFRP laminates. *Proc Eng*, 58:533-542. https://doi.org/10.1016/j.proeng.2013.05.061

Piekutowski AJ, 1993. Characteristics of debris clouds produced by hypervelocity impact of aluminum spheres with thin aluminum plates. *Int J Impact Eng*, 14(1-4):573-586. https://doi.org/10.1016/0734-743X(93)90053-A

Summers JL, 1959. Investigation of High-Speed Impact: Regions of Impact and Impact at Oblique Angles. National Aeronautics and Space Administration, USA.

Teague MR, 1980. Image analysis via the general theory of moments. *J Opt Soc Am*, 70(8):920-930. https://doi.org/10.1364/JOSA.70.000920

Verma PN, Dhote KD, 2018. Characterising primary fragment in debris cloud formed by hypervelocity impact of spherical stainless steel projectile on thin steel plate. *Int J Impact Eng*, 120:118-125. https://doi.org/10.1016/j.ijimpeng.2018.05.003

Wang QT, Zhang QM, Huang FL, et al., 2014. An analytical model for the motion of debris clouds induced by hypervelocity impact projectiles with different shapes on multi-plate structures. *Int J Impact Eng*, 74:157-164. https://doi.org/10.1016/j.ijimpeng.2014.06.006

Watson E, Gulde M, Hiermaier S, 2017. Fragment tracking in hypervelocity impact experiments. *Proc Eng*, 204:170-177. https://doi.org/10.1016/j.proeng.2017.09.770

Watson E, Maas HG, Schäfer F, et al., 2018. Trajectory based 3D fragment tracking in hypervelocity impact experiments. *Int Arch Photogramm Remote Sens Spat Inform Sci*, XLII-2:1175-1181.

https://doi.org/10.5194/isprs-archives-XLII-2-1175-2018

Yin C, Dadras S, Huang XG, et al., 2019. Optimizing energy consumption for lighting control system via multivariate extremum seeking control with diminishing dither signal. *IEEE Trans Autom Sci Eng*, 16(4):1848-1859. https://doi.org/10.1109/TASE.2019.2901432

Yin C, Dadras S, Cheng YH, et al., 2020. Multidimensional fractional-order Newton-based extremum seeking for online light-energy saving technique of lighting system. *IEEE Trans Ind Electron*, 67(10):8576-8586. https://doi.org/10.1109/TIE.2019.2950867

Zhang Q, Chen Y, Huang F, et al., 2008. Experimental study on expansion characteristics of debris clouds produced by oblique hypervelocity impact of LY12 aluminum projectiles with thin LY12 aluminum plates. *Int J Impact Eng*, 35(12):1884-1891. https://doi.org/10.1016/j.ijimpeng.2008.07.026